Acta Cryst. (1985). B41, 248-254

Diffuse Scattering of Fast Electrons in Barium Titanate

BY C. J. ROSSOUW

CSIRO Division of Chemical Physics, PO Box 160, *Clayton, Victoria* 3168, *Australia*

AND L. A. BURSILL

School of Physics, University of Melbourne, Parkville, Victoria 3052, *Australia*

(*Received* 6 *November* 1984; *accepted* 20 *March* 1985)

Abstract

Dynamical electron diffraction theory is used to explain structure in diffuse-scattering patterns from barium titanate. A point-scattering model as well as an Einstein model for TDS is used to account explicitly for the effects of scattering from each atomic site within the unit cell. The angular dependence of TDS indicates a significant contribution from O sites. Effects of static atomic displacements corresponding to the paraelectric/ferroelectric phase transition at *ca* 413 K are investigated on a point-scattering model. Ability to concentrate current density on specific crystallographic sites may provide a powerful tool for the investigation of thermal scattering mechanisms.

1. Introduction

The intensity distribution of thermal diffuse scattering (TDS) in electron diffraction patterns is related to the coupling between dynamical elastic and inelastic wavefunctions ψ and ψ' which describe the fast electron in the crystal (Rossouw & Bursill, 1985). Application of this theory to investigate the relationship between observed diffuse scattering from $BaTiO_3$ and localized sources of inelastic scattering is presented in this paper. There is some analogy with the ALCHEMI technique for site location of specific ionized species through the orientation dependence of X-ray emission or characteristic losses in energy-loss spectra [see, for instance, Spence & Taftø (1982) and Taftø & Krivanek (1982)]. Descriptions of Kikuchi-line or Kossel-line formation (Gjønnes & Taftø, 1976; Ichimiya & Lehmpfuhl, 1978) have been based on anomalous absorption acting independently on each Bloch-wave component of ψ, applicable to multiple scattering from thick crystals. In the single scattering theory for relatively thin crystals presented in this paper, dynamical effects are accounted for by the natural peaking and diminishing of $|\psi|^2$ on localized scattering sites as a function of thickness and orientation. A unified treatment of dynamical effects induced in ionization and TDS from thin crystals has been given by Rossouw (1985).

If the incident electron wavevector $\mathbf{k}$ is parallel to a low-index zone axis, electron current density J associated with ψ tends to peak on atom sites. Within a small range of scattering angles θ (or momentum transfers $\hbar\mathbf{q}$), current density J' associated with ψ' may be similarly peaked on these sites in the crystal, leading to dynamically enhanced coupling between ψ and ψ' *via* a localized scattering potential. This leads to the formation of excess Kikuchi bands. The edge of an excess band is defined by the crystal orientation where maxima in J' move away from atom sites, leading to dynamical decoupling for the $\psi \rightarrow \psi'$ transition. As shown below, this condition often coincides with the position of Brillouin-zone (BZ) boundaries in diffraction patterns.

Rossouw & Bursill (1985) have shown how the Einstein model for TDS can be incorporated in a full n-beam dynamical scattering model. We use a modified version of this model to correlate the angular dependence of TDS from $BaTiO_3$ with theoretical predictions. The angular variation of current density on specific atomic sites is also calculated, along with the variation above and below the ferroelectric transition temperature T_f.

2. Experimental

Lamellar-shaped as-grown crystals of $BaTiO_3$, about 0·3 mm thick, were provided by Professor J. Harada. These were mechanically polished to 60–80 μm prior to chemical thinning in hot orthophosphoric acid. Clean low-angle wedge-shaped crystals were selected and examined in a JEOL-100CX using a high-tilt goniometer for recording diffraction patterns at room temperature. By ensuring that the region within the selected-area aperture was not bent, diffraction patterns from [001] and [1$\bar{1}$0] zone axes were obtained without smearing the fine structure in TDS over a range of angles. Usually a series of patterns from one area was recorded, with exposure times between 1 and 64 s. Kikuchi patterns were obtained from relatively thick areas, $t \approx 200$ nm.

Fig. 1 shows a [001] pattern: note the excess inner square of diffuse intensity with four {100} beams as

0108-7681/85/040248-07$01.50

vertices, and other less intense features associated with {200} beams. Optical phonon scattering should give, for correlation lengths of 3 nm or more, very sharp streaks which would be relatively insensitive to crystal tilt (Cowley, 1981). The observed Kikuchi bands and other fine structure moved with crystal tilt, and should therefore arise from localized inelastic interactions. Fig. 2 shows a $[1\bar{1}0]$ pattern from an area which included some ferroelectric domain walls. Deficit scattering occurs around 000, together with a complex Kikuchi structure. Sharp diffuse streaks occur parallel to [110], through 002 and $00\bar{2}$. These are insensitive to tilt and probably represent longitudinal optical phonon modes. An experimental study of the temperature dependence of these will be reported separately.

3. Theory

A Bloch-wave description of TDS, using an Einstein scattering model, was developed by Hall & Hirsch (1965), where scattering from a two-beam elastic state to a plane-wave final state was considered. This theory was extended by Rossouw & Bursill (1985) to account for n-beam dynamical effects in both ψ and ψ'. Such a description leads to a severe limitation on the number of Bragg beams in the calculation with present computing facilities. This number can be increased from about 9 to a more respectable 45 beams or so by assuming ψ to be a plane wave. Consequences of this approximation are discussed in § 6(a). Crystal orientation with respect to ψ is constant but orientation of ψ' varies with scattering angle θ. Dynamical structure relates to the orientation dependence of J' on localized scattering centres. The expression for the intensity scattered per unit solid angle may then be written, from equations (1-5) of Rossouw & Bursill (1985), as

$$\frac{\mathrm{d}I}{\mathrm{d}\Omega} = nt \sum_{gh} [\text{site}]\,[\text{kin}] \sum_{ij} C_0^i C_0^{j*} C_g^{i*} C_h^j X^{ij}(t), \qquad (1)$$

where terms describing diffraction in the initial state are discarded. Here n is the number of lattice sites per unit volume and t the crystal thickness. Reciprocal-lattice vectors $\mathbf{g}, \mathbf{h}$ refer to diffracted beams in ψ', and the branch indices i, j to dispersion surfaces. The C's are the Bloch-wave eigenvectors, with eigenvalues γ^i. The t-dependent interference term $X^{ij}(t)$ is related to separation of the inelastic dispersion surfaces by the expression

$$X^{ij}(t) = \{\exp[i(\gamma^i - \gamma^j)t] - 1\}/it(\gamma^i - \gamma^j). \qquad (2)$$

The [site] term is summed over the m atoms of type α in the unit cell, *i.e.*

$$[\text{site}] = \sum_{\alpha} \sum_{m} \exp[i(\mathbf{h}-\mathbf{g}) \cdot \boldsymbol{\tau}_{\alpha m}], \qquad (3a)$$

where $\boldsymbol{\tau}$ is a position vector of an atom in the unit cell. The term describing the TDS interaction is (Rossouw & Bursill, 1985; see Appendix)

$$[\text{kin}] = f_\alpha(\mathbf{q}-\mathbf{h}) f_\alpha^*(\mathbf{q}-\mathbf{g}) \{\exp[-M_\alpha(\mathbf{h}-\mathbf{g})] - \exp[-M_\alpha(\mathbf{q}-\mathbf{g}) - M_\alpha(\mathbf{q}-\mathbf{h})]\}, \qquad (3b)$$

where the Debye-Waller terms are defined as

$$M(\mathbf{Q}) = \tfrac{1}{2} Q^2 \langle u_\alpha^2 \rangle, \qquad (4)$$

with $\langle u_\alpha^2 \rangle$ the mean-square displacement from equilibrium along wavevector $\mathbf{Q}$, and $f(\mathbf{Q})$ the atomic scattering amplitude. The combined factor [site] [kin] is equivalent to the form factor for inelastic scattering (Kainuma, 1955). Equation (1) reduces to the current density (apart from the term nt), summed over sites $\boldsymbol{\tau}$, if the [kin] term is set equal to unity for all $\mathbf{q} = \mathbf{k} - \mathbf{k}'$,

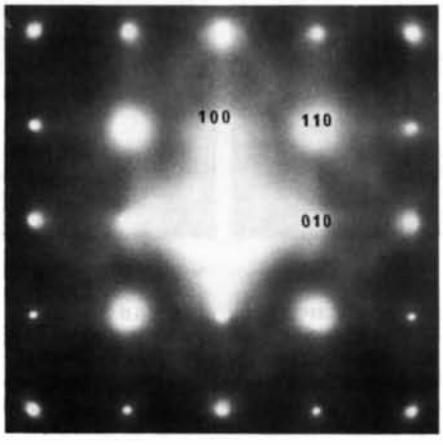

Fig. 1. TDS from $BaTiO_3$, [001] zone axis.

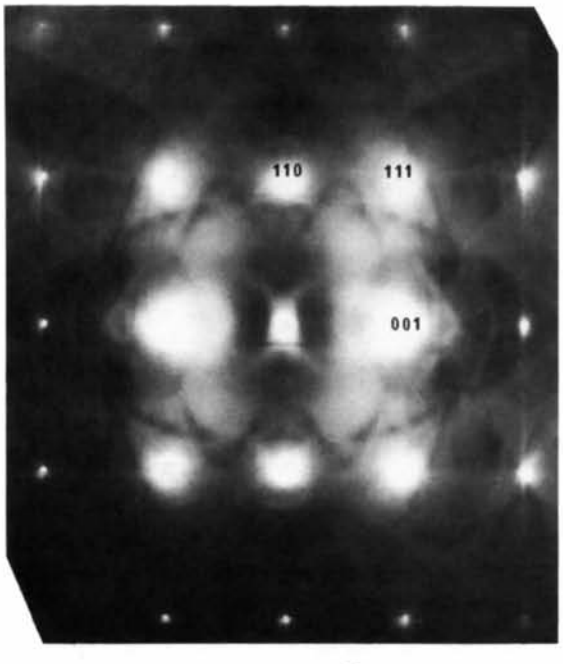

Fig. 2. TDS from $BaTiO_3$, $[1\bar{1}0]$ zone axis.

where $\mathbf{k}'$ is the wavevector associated with ψ'. Relativistic relationships between $\mathbf{k}$, $\mathbf{q}$ and θ [see, for instance, Rossouw & Maslen (1984)] were used in the calculations.

Orientation of the inelastic beam is most conveniently described by the intercept of the centre of the Laue circle with the reciprocal lattice. If the orientation of ψ is $[uvw]$, the orientation of ψ' for a point $\mathbf{p}$ on the diffraction pattern is

$$[u'v'w'] = [uvw] - \mathbf{p}. \qquad (5)$$

In the following text this brief notation $[u'v'w']$ defines orientation. For systematic row excitations, this point bisects the vector from the origin to the intercept of the reciprocal lattice with the Ewald sphere. Momentum transfer $\hbar\mathbf{q}$ to the crystal is antiparallel to $\mathbf{p}$, and, at least for small energy transfers associated with TDS, $\mathbf{p} \approx -\mathbf{q}$. Projections of the crystal structure down [001] and [1$\bar{1}$0] zone axes are shown in Figs. 3(a) and 3(b).

4. Current density

Current density associated with the fast electron varies with crystal orientation and position in the unit cell. This may be related to dynamical effects in the diffusely scattered distribution by calculating current density on various sites as a function of orientation. In the simplest approximation of δ-function potentials, this is equivalent to mapping the thickness-averaged signal from incoherently emitting sources of spherical waves located on the various atom sites. We map J' as a function of orientation on these sites, and orientations of interest are subsequently chosen to demonstrate how current density in the unit cell varies with orientation. 45 beams were included in each calculation.

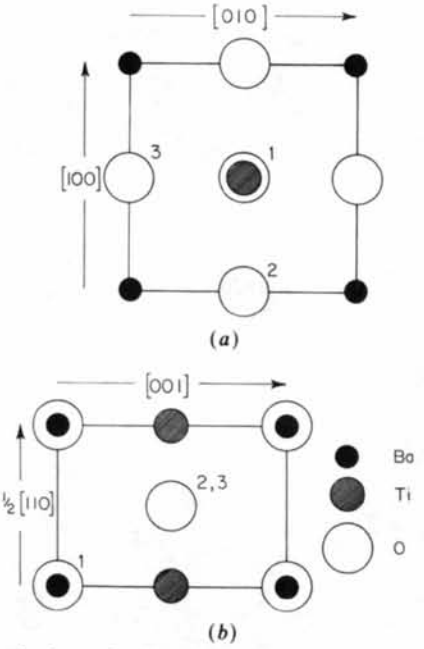

Fig. 3. Projections of cubic $BaTiO_3$ structure down (a) [001] zone, (b) [1$\bar{1}$0] zone.

4(a). *Orientation dependence of current density*

Fig. 4 maps angular variations in current density on Ba, Ti and O(2) for [001]. Dynamically generated structure is related to a projection of fast-electron BZ boundaries onto the diffraction pattern, since a rapid fluctuation in current density on a specific site often occurs just as a diffracted beam is brought into the exact Bragg orientation. This coincides with the component of the inelastically scattered wavevector $\mathbf{k}'_g$ along $\mathbf{g}$ being $\mathbf{k}'_g = -\frac{1}{2}\mathbf{g}$. With the elastic orientation [000], the BZ boundaries bisect $\mathbf{g}$, $\mathbf{h}$ in the diffraction pattern, and are often rendered visible by a transition from excess to deficit scattering.

Maxima in current density on Ba with tilt along [110] (Fig. 4a) correspond to scattering towards adjacent Ti and O(1) atomic columns. Weaker coupling towards O(2, 3) occurs when the crystal is tilted along [100]. On the other hand, scattering from Ti (Fig. 4b) is not strongly enhanced when tilted towards either nearest-neighbour atoms. For O(2) in Fig. 4(c), broad streaking towards adjacent Ti and O(1) atom columns occurs with tilt along [100], with a well defined maximum connecting the 000 and 100 beams. Deficit

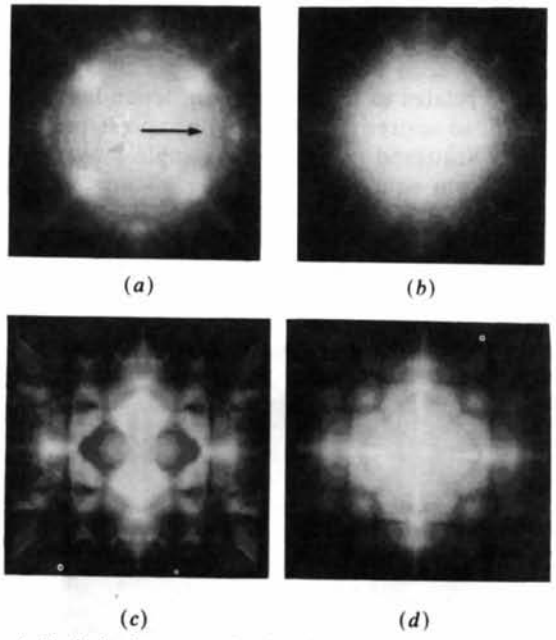

Fig. 4. Variation in current density of ψ' on different sites, projected onto a [001] diffraction pattern, with $\mathbf{g}_{010}$ arrowed in (a). The maximum and minimum current densities are given within parentheses (max., min.). (a) Ba site (3·0, 1·07), (b) Ti and O(1) (4·09, 1·11), (c) O(2) (6·03, 0·38), (d) summation over all three O sites (14·2, 2·19). The minimum is subtracted from each distribution for greater display clarity.

scattering towards Ba occurs if the crystal is tilted along the orthogonal [010] direction. Here BZ boundaries are brought into contrast by rapid fluctuations in J' with orientation. The summation of current densities on all three O sites is shown in Fig. 4(*d*). Not surprisingly, coupling along ⟨100⟩ towards nearest-neighbour atoms is evident. The end of each 'streak' corresponds to the position of an elastic 100 beam in the diffraction pattern, where the $\bar{2}00$ beam in ψ' is in the exact Bragg condition.

For the [1$\bar{1}$0] projection, the Ba site projects onto O(1), and the remaining two O sites overlap (Fig. 3*b*). The angular variation on Ba and O(1) (Fig. 5*a*) shows broad maxima for tilt along [001] and weaker maxima with tilt along [110]. Ti in Fig. 5(*b*) shows monotonically decreasing J' with increasing θ, and O(2, 3), in Fig. 5(*c*), has maxima at wide angles for tilts along [110] towards Ti, peaking at $\mathbf{p} = 0{\cdot}83$ [110]. This result was used to predict this orientation which maximizes J' on O(2, 3), thus 'pumping' this site with excess current density (*cf.* Fig. 6*d*).

4(*b*). *Distribution of current density in the unit cell*

Fig. 6(*a*) shows current density for a symmetrical orientation along [001]. The relatively large maxima which occur on O(2, 3) compared with Ba are an artefact due to the calculation being limited to 45 beams, and J' on Ba approaches that on O(2, 3) if the number of beams in the calculation is increased. Maxima break away from Ti and O(2, 3) at $\mathbf{p} = 0{\cdot}73$ [110] in Fig. 6(*b*), corresponding to a maximum of J' on Ba in Fig. 4(*a*). For the symmetrical orientation along [1$\bar{1}$0] (Fig. 6*c*), maxima occur on Ti, with weaker maxima on Ba and O(2, 3). Maxima move onto O(2, 3) at an orientation 0·83 [110] in Fig. 6(*d*), as derived from Fig. 5(*c*).

4(*c*). *Variations in current density in the ferroelectric phase*

The paraelectric cubic phase becomes tetragonal at temperatures below T_f, with electric polarization vector **P** parallel to one of the original ⟨100⟩ axes. The unit-cell parameters change from $a = 4{\cdot}01$ Å to $a_t = 3{\cdot}99$, $c_t = 4{\cdot}03$ Å. Ba is now at $(0, 0, z_{\mathrm{Ba}})$, Ti at $(\frac{1}{2}, \frac{1}{2}, \frac{1}{2} + z_{\mathrm{Ti}})$, and O at $(\frac{1}{2}, \frac{1}{2}, z_1)$, $(\frac{1}{2}, 0, \frac{1}{2} + z_2)$ and $(0, \frac{1}{2}, \frac{1}{2} + z_2)$. Here $z_{\mathrm{Ba}} = 0{\cdot}018$, $z_{\mathrm{Ti}} = 0{\cdot}032$, $z_1 = -0{\cdot}007$ and $z_2 = -0{\cdot}003$ (Megaw, 1973). Complex eigenvectors for this non-centrosymmetric crystal were then calculated in order to compare the peaking of current density in the two phases. However, the orientation dependence of J' on atomic sites in the [1$\bar{1}$0] projection, with **P** at either 45 or 90° to this axis, was virtually indistinguishable for the two phases. For [001], scattering from O(2) towards Ti, perpendicular to **P**, as shown in Fig. 7(*a*) is somewhat diminished for the ferroelectric phase. The maximum value for current density in this plot is 3·78, compared with 6·03 in Fig. 4(*c*). The summed current-density distributions from all O sites are given in Fig. 7(*b*), where the streak perpendicular to **P** is diminished compared to that expected from the paraelectric phase in Fig. 4(*d*).

Thus, even for the most sensitive case of atoms acting as point-scattering sources within the unit cell, the effect of static displacements on the diffuse-scattering pattern is not marked. However, observations suggest that larger cross sections for TDS occur just above T_f.

5. Einstein TDS computations

Various values of r.m.s. atom displacements are available from X-ray or neutron diffraction data (see Ehses, Bock & Fischer, 1981). At 400 K, isotropic r.m.s. displacements along a particular direction are 0·079 Å for Ba, 0·097 Å for Ti and 0·092 Å for O. However, since at this stage we are interested in the angular distribution of scattering and not in absolute magnitudes, an isotropic r.m.s. displacement of 0·07 Å for all atoms at room temperature was assumed. Equation (1) was thickness-averaged by considering a branch-index summation over terms with $i = j$.

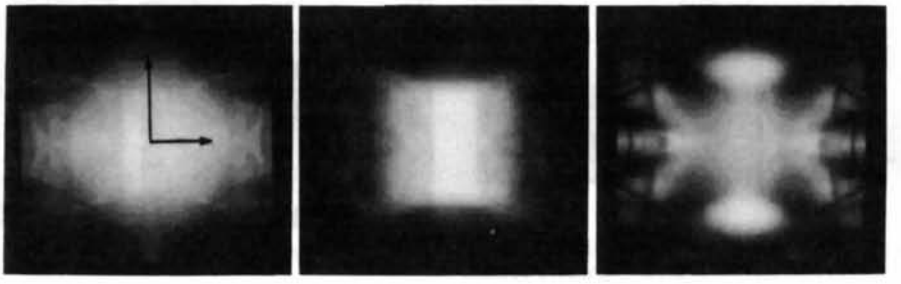

(*a*) (*b*) (*c*)

Fig. 5. Variation in current density of ψ' on different sites, projected onto a [1$\bar{1}$0] diffraction pattern, with $\mathbf{g}_{001}$ (horizontal) and $\mathbf{g}_{110}$ (vertical) indicated in (*a*). The maximum and minimum current densities are given within parentheses (max., min.). (*a*) Ba and O(1) (4·42, 1·09), (*b*) Ti site (5·94, 0·42), (*c*) O(2, 3) (3·6, 0·38). The minimum is subtracted from each distribution for greater display clarity.

Fig. 8 shows computed results for the [001] projection, where dynamical features in Fig. 4 are somewhat altered by changing the [kin] term from δ-function scattering to the Einstein form for TDS. The central minimum is typical for this description of TDS. In Fig. 8(a), strong features from the Ba site occur at the first 110 BZ boundaries with {100} beams as vertices, with streaking between the first and second BZ boundaries from $[\frac{1}{2}\frac{1}{2}0]$ to [110]. TDS from Ti in Fig. 8(b) has intersecting 100 and 110 (and higher-order) BZ boundaries contributing to dynamical structure.

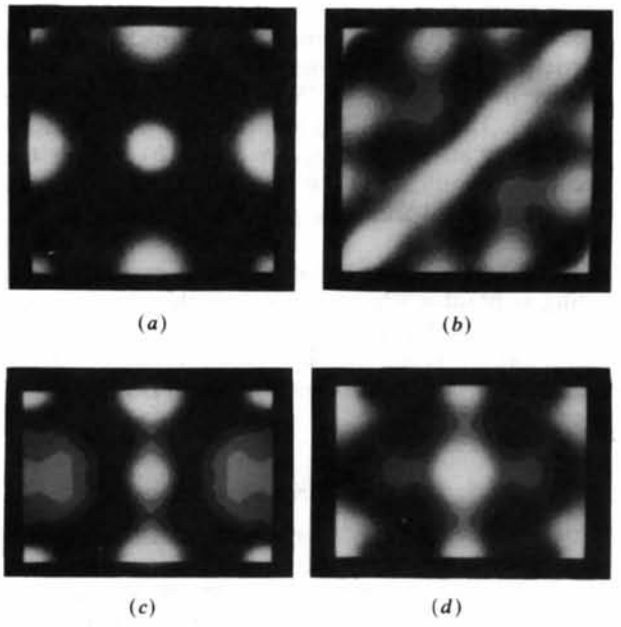

(a) (b) (c) (d)

Fig. 6. The distribution of current density within the crystal viewed down the [001] axis. (a) Symmetrical orientation (5·8, 0·29) and (b) orientation 0·73 [110] (2·53, 0·37). The [1$\bar{1}$0] projection is shown in (c) symmetrical orientation (5·61, 0·24), and (d) orientation 0·83 [110] (3·61, 0·35). The minimum value is subtracted from each distribution to enhance clarity.

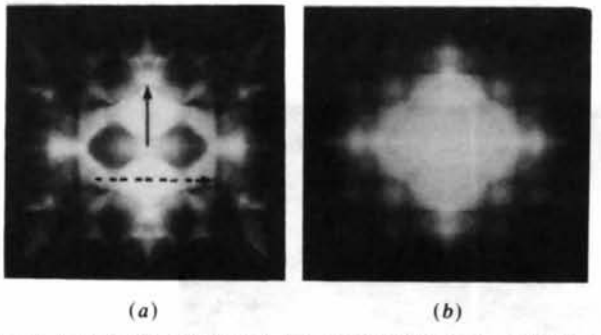

(a) (b)

Fig. 7. (a) Computed current density on O(2), projected onto a [001] diffraction pattern, with $BaTiO_3$ in the tetragonal ferroelectric phase. The polarization vector **P** is indicated by the dashed line, orthogonal to the arrowed vector $\mathbf{g}_{100}$. The maximum and minimum values are (3·78, 0·45). (b) is the summation from all O sites (11·6, 2·22). The minimum value is subtracted from each distribution for greater clarity.

Maxima in TDS from O(2) in Fig. 8(c) take place well away from low-order BZ boundaries, *i.e.* dynamically enhanced scattering from these sites takes place at larger tilts from the [001] zone axis. The summation of intensity from all sites, but scaled by a factor μ_α^{-1}, where μ_α is the mass of atom α, is shown in Fig. 8(d). Such scaling is discussed in § 6(d), but appears necessary to increase the intensity from O compared with other species. Correlation between Figs. 1 and 8(d) is evident, after allowing for elastic Bragg beams not being included in the TDS calculation.

For a [1$\bar{1}$0] zone axis, scattering from Ba in Fig. 9(a) has some of the features of the point-scattering distribution (Fig. 5a), although the TDS from Ti in Fig. 9(b) is not similar to Fig. 5(b). TDS from O(2, 3) (Fig. 9c) has some features comparable with those in Fig. 5(c). The summed response from all sites, scaled by μ_α^{-1}, is shown in Fig. 9(d). This correlates fairly well with the observed Kikuchi-line pattern in Fig. 2. Scattering inwards from {111} beams towards the central beam is predicted, as well as deficient scattering along [110] and [001].

6. Discussion

6(a). *Limitations due to use of a plane-wave* ψ

Current density in Figs. 6(a) and 6(c) is associated with 100 keV electrons incident along [001] or [1$\bar{1}$0]

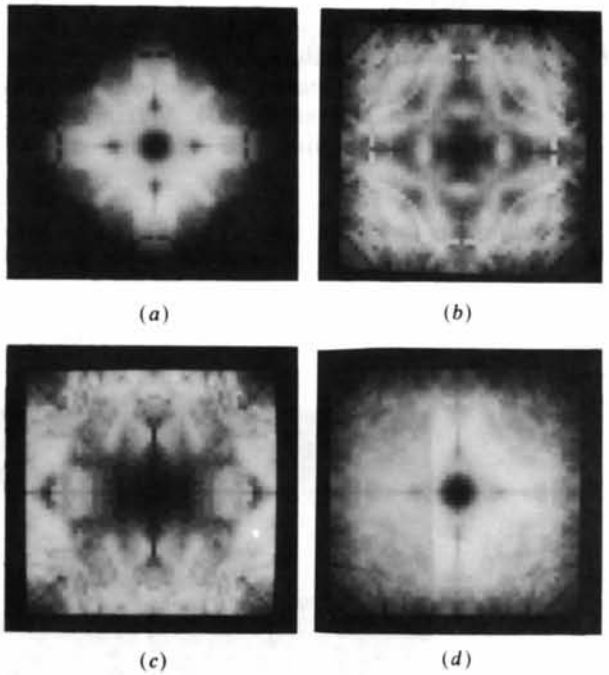

(a) (b) (c) (d)

Fig. 8. Einstein TDS computations of dynamical effects superimposed on a [001] diffraction pattern (with scaling factor and orientation as defined in Fig. 4). (a) Ba contribution, (b) Ti and (c) O site 2. (d) shows the summation from all sites, modulated by μ_α^{-1}.

zone axes. Describing ψ as a plane wave means that we consider the crystal to be flooded with a uniform current density J associated with the incident state. However, we have accounted for the effect of variations of J' associated with the final state. For point-source scattering, describing both ψ and ψ' dynamically would simply multiply the orientation dependence of J' by J (associated with ψ on that source), leaving the angular distribution unaltered. For more realistic scattering potentials, however, some subtle effects resulting from spatial variations in J and their influence on scattered intensities are discarded in our calculations. Many-beam calculations, with a dynamical description of both ψ and ψ', have been performed for rutile with 9 beams (Rossouw & Bursill, 1985) but, for symmetrical orientations, first-order BZ boundaries alone are accounted for. It is not possible to complete fully dynamical 45-beam distributions, given finite computing resources.

6(*b*). *Extension to phonon models*

The Einstein model approximates thermal motion to atomic displacements uncorrelated in time, so that, after time-averaging, each atom acts as an independent scattering source. The first-order phonon model should be valid for small-angle scattering from Bragg beams, where low-frequency acoustic phonons provide the dominant contribution. However, for $q > g/2$, higher-order phonon effects contribute to TDS at larger angles (Rez, Humphreys & Whelan, 1977). In contrast, the Einstein model is valid for all scattering angles. Given that phonon lifetimes and spatial correlation lengths are usually very short, it is reasonable to expect that the Einstein model should adequately describe the wide-angle TDS generated by localized scattering events. Diffuse streaks due to phonon modes are readily distinguishable from dynamical effects, since these do not move across the diffraction pattern with crystal tilt (*cf.* Fig. 2).

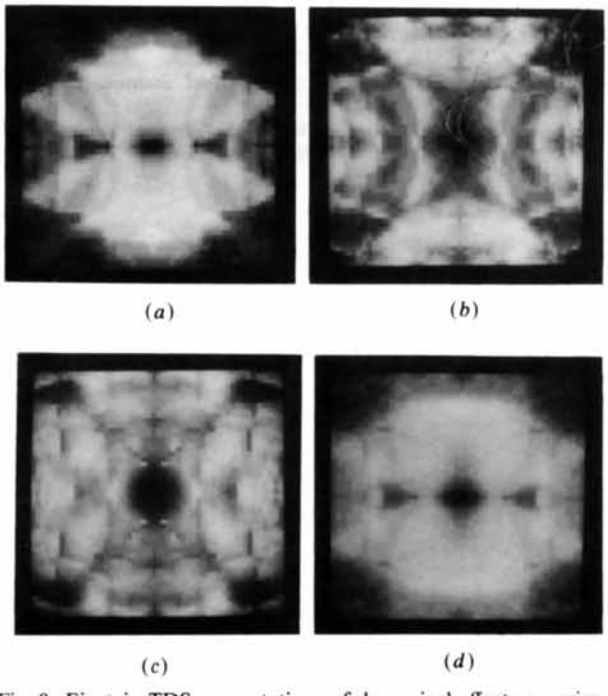

Fig. 9. Einstein TDS computations of dynamical effects superimposed on a [1$\bar{1}$0] diffraction pattern (with scaling factor and orientation as defined in Fig. 5). (*a*) Ba contribution, (*b*) Ti and (*c*) O sites 2 and 3. (*d*) shows the summation from all sites, modulated by μ_α^{-1}.

6(*c*). *Energy filtering of the diffraction pattern*

Ideally the diffraction pattern should be energy filtered so that elastic Bragg beams and quasi-elastic TDS alone may be studied (Philip, Whelan & Egerton, 1974). Inelastic plasmon and single electron excitations are sharply peaked about Bragg beams, with a Lorentzian angular distribution of half-width $E/2E_0$ (Egerton, 1976), where E is the energy transfer and E_0 the incident-beam energy. This is typically a few tenths of a milliradian. Thus, within the single scattering regime, TDS remains the dominant mechanism for wide-angle scattering. Finite convergence in electron diffraction patterns, in particular for convergent-beam diffraction, may introduce convolution between plasmon and thermal scattering. This was avoided by the use of point diffraction patterns.

6(*d*). *Comparison with experiment*

With equal r.m.s. displacements of 0·07 Å, the ratio of peak scattering in the Einstein TDS distribution Ba:Ti:O is approximately 40:5:1. The Einstein model reproduces the gross features of TDS for the two projections studied only if contributions from O are given significantly more weight than this. A similar conclusion was reached following comparison of experimental and calculated TDS patterns of rutile (Rossouw & Bursill, 1985).

The effects of variations of the incident-state current density on different atomic sites (Fig. 6) are certainly not strong enough to explain the apparent predominance of thermal scattering from O. In any case, these were accounted for by a full dynamical (9-beam) treatment in the case of rutile. Predominant vibrational modes for rutile and barium titanate often give displacements lying parallel to the projection axis; thus heavier Ba and Ti atoms may appear to vibrate 'in phase' rather than 'at random', at least over distances of the order of the lateral coherence length of the fast electron. Use of a phonon model, rather than an Einstein model, may be necessary. As shown by Rez, Humphreys & Whelan (1977) or Willis & Pryor (1975) the displacement from equilibrium of an atom α, for a particular phonon wavevector and polarization, contains a term $\mu_\alpha^{-1/2}$; thus the scattered

intensity from phonons is modulated by terms μ_α^{-1}. Electronic polarization excited within the crystal by the electron probe has not been accounted for. This may become significant in materials with exceptionally high dielectric constants (*e.g.* $\varepsilon/\varepsilon_0 \approx 100$ for TiO_2, ≈ 1200 for $BaTiO_3$).

The electron probe will impart thermal energy to the atoms and, since this process is not in thermal equilibrium, bulk r.m.s. displacement values may not apply. A scaling factor μ_α^{-1} may again be appropriate, enhancing the contribution from the lighter atoms (this amounts to an artificial probe-induced temperature factor). Use of this scaling factor improved correlation of the summed TDS from all sites with experiment.

The present work has demonstrated the value of understanding the orientation dependence of enhanced or diminished scattering from particular individual sites. Use of a dynamically generated site-dependent probe, with calculations of the angular distribution of TDS, may ultimately prove more powerful than the study of thermal vibrations by monitoring Bragg intensities alone. Kinematical approximations provide a simpler analytical framework, but the agreement obtained by a parameterized fit of Bragg data may be misleading when dealing with localized scattering effects. The ability to 'pump' current density selectively onto certain crystal sites by appropriate choice of diffraction conditions may well be valuable for the study of the occupancy of multiple-well sites, premonitory to structural phase transitions in solids.

Modelling of TDS on a multiple phonon description, as well as the inclusion of polarization effects and a full Bloch-wave scattering model, is necessary for further analysis. Even on the Einstein model, modelling of TDS is limited by our computing resources.

This work was supported by a joint CSIRO-University of Melbourne collaborative research grant. We are grateful to Peng Ju Lin and Peter Hanan for help with some of the experimental work.

References

COWLEY, J. M. (1981). *Diffraction Physics*, 2nd ed., pp. 150, 249-261. New York: North-Holland.

EGERTON, R. F. (1976). *Philos. Mag.* **34**, 49-56.

EHSES, K. H., BOCK, H. & FISCHER, K. (1981). *Ferroelectrics*, **37**, 507-510.

GJØNNES, J. & TAFTØ, J. (1976). *Nucl. Instrum. Methods*, **132**, 141-148.

HALL, C. R. & HIRSCH, P. B. (1965). *Proc. R. Soc. London Ser. A*, **286**, 158-177.

ICHIMIYA, A. & LEHMPFUHL, G. (1978). *Z. Naturforsch. Teil A*, **33**, 269-281.

KAINUMA, Y. (1955). *Acta Cryst.* **8**, 247-257.

MASLEN, V. W. & ROSSOUW, C. J. (1983). *Philos. Mag.* **47**, 119-130.

MEGAW, H. (1973). *Crystal Structures: A Working Approach*, p. 290. London: W. B. Saunders.

PHILIP, J. G., WHELAN, M. J. & EGERTON, R. F. (1974). *Eighth International Congress on Electron Microscopy*, Vol. 1, pp. 276-277. Canberra: Australian Academy of Science.

REZ, P. HUMPHREYS, C. J. & WHELAN, M. J. (1977). *Philos. Mag.* **35**, 81-96.

ROSSOUW, C. J. (1985). *Ultramicroscopy*. In the press.

ROSSOUW, C. J. & BURSILL, L. A. (1985). *Acta Cryst.* A**41**, 320-327.

ROSSOUW, C. J. & MASLEN, V. W. (1984). *Philos. Mag.* **49**, 743-758.

SPENCE, J. C. H. & TAFTØ, J. (1982). *Scanning Electron Microscopy*, Vol. 2, pp. 523-531. Chicago: SEM Inc.

TAFTØ, J. & KRIVANEK, O. L. (1982). *Nucl. Instrum. Methods*, **194**, 153-158.

WILLIS, B. T. M. & PRYOR, A. W. (1975). *Thermal Vibrations in Crystallography*, p. 43. Cambridge Univ. Press.